Nonlinear adjustment of density fronts. Part 1. The Rossby scenario and the experimental reality

By A. STEGNER[1], P. BOURUET-AUBERTOT[2]
AND T. PICHON[3]

[1]Laboratoire de Météorologie Dynamique, IPSL, ENS, 24 Rue Lhomond, 75005 Paris, France
stegner@lmd.ens.fr

[2]Laboratoire d'Océanographie Dynamique et Climatologique, IPSL, Université Pierre et Marie Curie,
Jussieu, 75252 Paris Cedex 05, France
pba@lodyc.jussieu.fr

[3]UME, ENSTA Centre de l'Yvette, Chemin de la huniere, 91120 Palaiseau Cedex, France

This study deals with the nonlinear cyclo-geostrophic adjustment of a circular density front in a two-layer fluid. Laboratory experiments have been performed to investigate the dynamical evolution of a fixed volume of buoyant water, initially confined within a bottomless cylinder, which is quickly released in a dense rotating fluid. This configuration corresponds to a rapid input of potential energy in a geostrophic fluid layer and reproduces some dynamical processes which occur during oceanic upwelling or stratospheric warming events. We focus our efforts on the visualization techniques in order to have simultaneous and independent measurements of both the horizontal velocity field and the vertical density field. We thus obtained, for the first time, quantitative measurements of the potential vorticity and the flow balance after a geostrophic adjustment process. The density profile of the mean adjusted state observed in the experiment is in good agreement with the prediction of the standard adjustment theory based on Lagrangian conservation of potential vorticity except in the frontal region. There, strong three-dimensional motions (plume structures, shocks and rapid transient instabilities) take place during the early stage of adjustment. These transient three-dimensional motions could dissipate up to 50% of the initial energy of the system, especially when the size of the initial density anomaly is close to or larger than the deformation radius. Therefore, it significantly changes the velocity and the energy budget predicted by the standard Rossby adjustment. Both the kinetic energy of the mean adjusted state and the energy transferred to inertia–gravity wave modes are reduced by these transient dissipative processes.

1. Introduction

The geostrophic adjustment is the first dynamical process which converts a significant fraction of the potential energy input (thermal or density source) of the atmosphere and the ocean into kinetic energy. During the rapid adjustment toward a quasi-equilibrium state, an important part of the initial energy could be transferred to inertia-gravity waves or dissipated through small-scale three-dimensional motions. These transient dynamical events play an important role in the inertia–gravity wave emission and local mixing in the vicinity of atmospheric jets and oceanic currents.

The first theoretical guidelines for solving geostrophic adjustment problems were proposed by Rossby (1938) and Obukhov (1949) in the framework of rotating shallow-water fluid (for a review see Blumen 1972). They assume that any initial unbalanced state will evolve naturally toward a steady balanced state, geostrophic or cyclo-geostrophic, satisfying mass and Lagrangian conservation of potential vorticity (PV). This approach conveniently avoids the time-dependent problem, and gives a prediction for the final state. However, the final energy of the predicted adjusted state is always less than the initial energy. Inertia–gravity waves, with zero PV, are then expected to carry the missing part of the initial energy away from the adjusted state (Gill 1982). This quantitative energy budget is the powerful result of this approach. More precisely the energy of the balanced state as well as the fraction of energy transferred to inertia–gravity waves mainly depend on the square of the ratio of the deformation radius (i.e. the Rossby radius) and the horizontal scale of the unbalanced state, namely a dimensionless Burger. Two cases are generally distinguished, the mass adjustment and the momentum adjustment. They correspond, respectively, to initial unbalanced states which contain only potential or kinetic energy. For the mass (momentum) adjustment, the energy lost to inertia–gravity waves is an increasing (decreasing) function of the Burger number (McWilliams 1988; Dewar & Killworth 1990; Boss & Thompson 1995; Kuo & Polvani 2000).

The question of fully nonlinear geostrophic adjustment in the rotating shallow-water framework has been recently revisited by means of theoretical (Ford, Norton & McIntyre 2000; Reznik, Zeitlin & BenJelloul 2001; Zeitlin, Medvedev & Plougonwen 2003) and numerical analysis (Kuo & Polvani 1997, 1999, 2000). These studies focus on the reversible–irreversible interactions between the waves and the mean adjusted flow. In particular, the formation of shocks, which seems to be a generic mechanism in the rotating shallow-water model, could strongly modify the classical scenario of geostrophic adjustment and the associated energy budget.

In this context, we performed laboratory experiments to investigate the nonlinear adjustment of a localized density anomaly in a rotating environment. A fixed volume of buoyant water, initially confined within a bottomless cylinder, is quickly released in a dense fluid. Similar experiments (e.g. Griffiths & Linden 1981; Bouruet-Aubertot & Linden 2002) and numerical simulations (Verzicco, Lalli & Campana 1997; Bouruet-Aubertot & Echevin 2002) were performed to study the baroclinic instability of a density front leading to meanders and eddies. As far as we know, a single work (Holford, 1994) studied the adjustment process in this experimental configuration. However, in this pioneering study, combined layer depth and velocity measurements were not possible. The present experiments were made with a slightly different range of parameters in order to prevent the growth rate of baroclinic disturbances during the adjustment process. We focused our efforts on the visualization techniques in order to have simultaneous and independent measurements of both the horizontal velocity field and the vertical density field. Therefore, we obtained, for the first time, quantitative measurements of the potential vorticity and the flow balance after a geostrophic adjustment process.

The mass adjustment performed in these experiments leads to a density front: the interface between the two fluids intersects the upper free surface. The geostrophic (Csanady 1979) or cyclo-geostrophic adjusted state (Flierl, 1979) calculated according to the Rossby adjustment theory contains a strong velocity discontinuity. Therefore, in this specific case, the predicted final state cannot be reached physically (i.e. for a dissipative fluid). Hence, our first objective will be to determine whether the system reaches a stable adjusted state and determine the balance of this state as well as the

potential vorticity conservation. Another important question we shall address deals with the energy budget of the adjustment process, taking into account dissipative and three-dimensional effects.

An overview of the paper follows. The experimental set-up and measurement techniques are presented in §2. After a brief dimensional analysis, physical parameters are introduced in §3. Then, in §4, we detail the approximations and the calculation of classical Rossby adjustment theory for an axisymmetric configuration corresponding to the laboratory experiments. The observed stages of the geostrophic adjustment are described in §5. Then, we analyse quantitatively in §6 the slow dynamics of the density anomaly averaged over one inertial period. The mean state obtained after the rapid transient process is compared with the predicted state calculated in §4. Besides, we analyse in detail the PV distribution and the balance of this mean adjusted state. The energy budget between the initial and the 'final' experimental state is evaluated in §7 and transient dissipative mechanisms are analysed. We give conclusions in §8.

2. Experimental set-up

The experiments were conducted on a 1.5 m diameter rotating turntable at the Department of Mechanics UME, ENSTA Palaiseau. The upper plate of this turntable rotates on a thin air layer in order to reduce friction and avoid all mechanical vibrations around the inertial frequency. The rotation rate Ω_0 could reach a value up to 12 r.p.m. We used a rectangular tank 48 cm large ($L = 24$ cm), 130 cm long and the working depth H was varied from 14 cm to 30 cm.

To obtain a cylindrical patch of fresh water confined within a transparent bottomless cylinder, we proceed as follows. We first waited until solid-body rotation of the dense fluid was reached, then we slowly introduced a fixed volume of fresh water inside the cylinder at the free surface level. We used three cylinders having a radius R_c of 3.45, 5.25 and 8.1 cm. These cylinders were made of a thin transparent film having a thickness around 0.2 mm to avoid strong volume perturbation during lift up. The initial thickness h_0 of this density anomaly was varied from 1 cm to 4 cm. The salinity of the lower layer was varied from 5 to 40 g l^{-1}.

In order to visualize a vertical cross-section of the density anomaly, the buoyant water was uniformly dyed with fluoresceine. The region where the buoyant water is located was then illuminated from above with a vertical laser sheet (figure 1). To optimize the fluorescent emission of the dye, we used an argon laser having a ray at 488 nm, which is close to 490 nm the maximum of absorption for fluoresceine in water. A CCD camera, fixed on the side of the tank, perpendicular to the laser sheet, was directly connected to a computer system with a frame-grabber card and the image-processing software NIH Image†. With this original non-intrusive technique, we were able to measure the displacement of the interface between the fresh and the dense water with an accuracy of 0.5 mm at an acquisition rate of 25 Hz. Besides, we could also measure the density field from the fluorescent dye emission (figure 2a). Indeed, on short time scale (i.e. the time scale of the experiment), the mixing of both dye and salt is expected to be driven mainly by convection (i.e. turbulent mixing). Hence, dye and salt gradient are not affected by relative diffusion and they are therefore proportional. In a first step, we measured the relative fluorescent light emission (figure 2b) which depends mainly on the dye concentration and the laser

† Free software developed at the US National Institutes of Health, available at http://rsb.info. nih.gov/nih-image/.

Vertical
laser sheet 488 nm

Transparent cylinder

Horizontal
laser sheet 670 nm

h_0

H

R_c

L

Pressurized
air flow

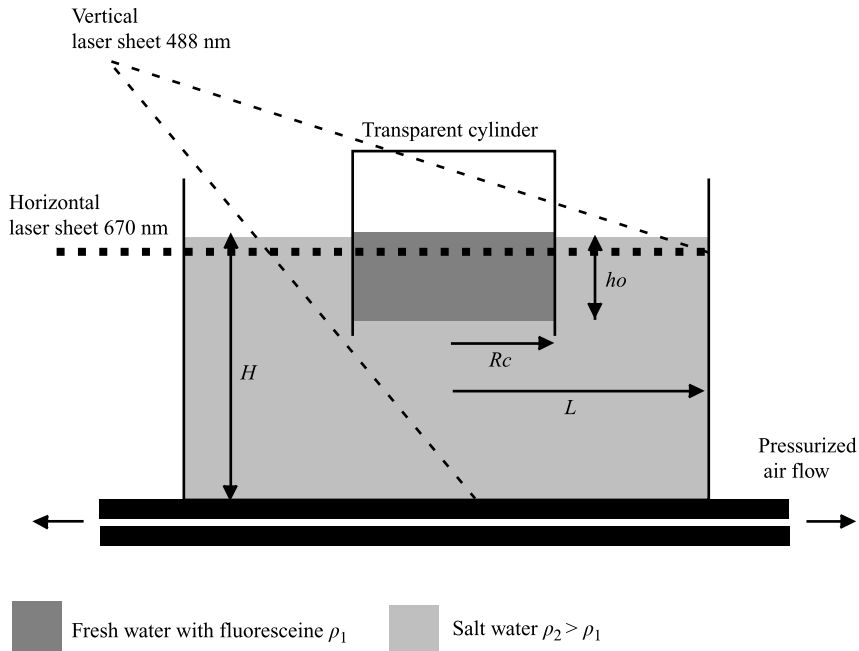Fresh water with fluoresceine ρ_1 Salt water $\rho_2 > \rho_1$

FIGURE 1. Sketch of the experimental aparatus.

sheet intensity. Then, taking into account the vertical distribution of the laser sheet intensity, we calibrated the light emission to deduce the vertical salinity profile in the lens (figure 2c). The continuous density profile was close to a two-layer configuration with a steep density gradient. The characteristic scale of this density gradient d could be estimated from the maximum slope of the vertical density profile (figure 2c). This density gradient thickness (2–5 mm) was relatively small compared to the initial lens thickness h_0 (1–4 cm).

In order to measure the horizontal velocity field, we used a horizontal laser sheet at 670 nm to lighten small neutral particles dispersed in the whole fluid volume and analyse the fluid motion with a standard particle image velocity (PIV) technique. For velocity measurements in the upper lens or the deep layer, the laser sheet was, respectively, focused 4 mm below the free surface or 2 cm below the transparent cylinder. For a few experiments, the horizontal PIV and the fluorescent visualization were used simultaneously. In this case, specific optic filters were fixed on each camera to detect only the dye emission in the vertical plane and the particles in the horizontal plane. We were then able to measure at the same time the horizontal velocity and the interface of the density lens. Hence, we obtained quantitative measurements on the flow balance after a geostrophic adjustment process.

3. Physical parameters

If we neglect the diffusion of salt and the viscous dissipation, the initial conditions are fixed by six physical scales, namely: h_0, H, R_c, L, $R_D = \sqrt{gH}/2\Omega_0$ the barotropic deformation radius and $R_d = \sqrt{g^*h_o}/2\Omega_0$ the baroclinic deformation radius, where $g^* = (\Delta\rho/\rho)g$ is the reduced gravity. For all experiments, the cylinder was located in the centre of the tank, far from the sidewall. The ratio R_c/L never exceeded 0.33 and we could reasonably neglect the boundary effects. Besides, the barotropic
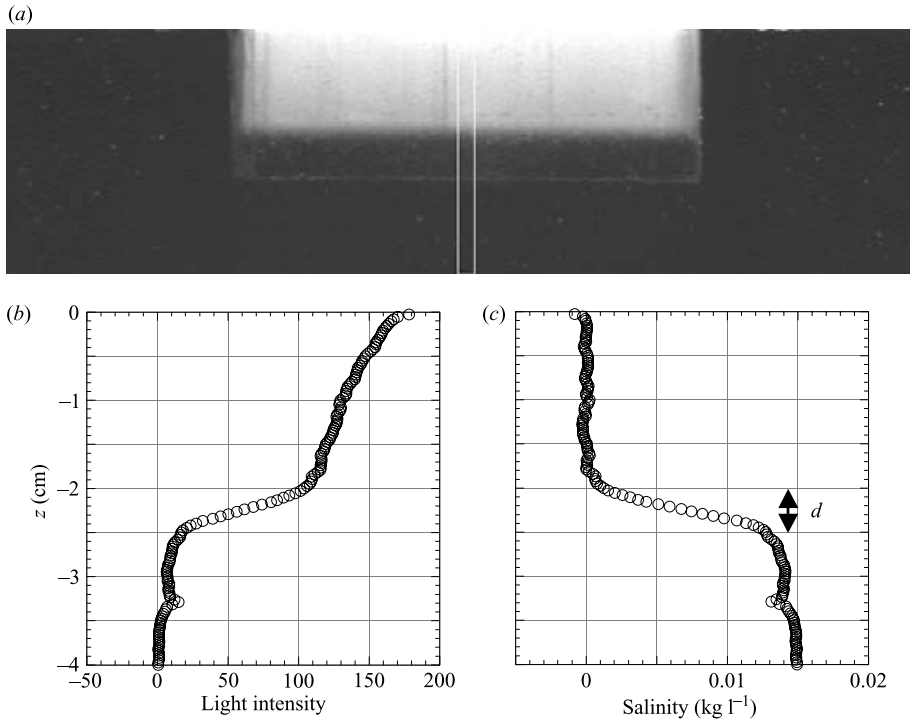
(a)

(b)

(c)

FIGURE 2. Measurement of the vertical salinity profile from the fluorescent light emission. (*a*) The fresh water initially confined in a transparent bottomless cylinder appears white owing to the fluorescent light emission and the dense water is black. (*b*) Vertical distribution of the light intensity in the central rectangle shown in (*a*). (*c*) The salinity profile can be deduced from (*b*) if we perform a careful calibration of the laser sheet intensity along the vertical plane. The disturbance at $z = -3.3$ cm is due to the light reflection at the bottom of the cylinder.

deformation radius R_D was always one or two order of magnitude larger than R_d and R_c. Hence, we assume that L and R_D have only a small impact on the evolution of the system. Therefore, according to dimensional analysis, the dynamical evolution of the density anomaly after the withdrawal of the cylinder is mainly governed by three dimensionless parameters. For comparison with previous studies, we introduce the Burgers number Bu, the vertical aspect ratio δ and the front steepness α:

$$Bu = \left(\frac{R_d}{R_c}\right)^2, \quad \delta = \frac{h_0}{H}, \quad \alpha = \frac{h_0}{R_d}.$$

In order to focus our study on the geostrophic adjustment, it was necessary to avoid or reduce the growth of baroclinic unstable modes (Griffiths & Linden 1981; Bouruet-Aubertot & Linden 2002) or barotropic gravity–Rossby modes (Hayashi & Young 1987; Sakai 1988; Paldor & Ghil 1991; Boss, Paldor & Thompson 1996) which could rapidly break the adjusted state. Therefore, we restricted our experiment to small aspect ratio only $\delta \sim 0.08$–0.1, while the Burgers number and the front steepness were varied in the following range of values: $Bu \sim 0.08$–1.5, $\alpha \sim 0.4$–1.2. For comparison, Holford (1994) investigated the nonlinear adjustment of a density anomaly with $\delta \sim 0.3$–0.6; $Bu \sim 0.05$–0.2 and $\alpha \sim 0.24$.

In order to estimate molecular dissipation and compare our experimental results with other experiments, we introduce a Reynolds number constructed with the

maximum velocity and the Rossby deformation radius:

$$Re = \frac{V_{\max} R_d}{\nu}.$$

The following results were obtained with Reynolds number in the range $Re \sim 250$–700.

4. Rossby adjustment model for axisymmetric density front

In this section, we present the approximations and the calculation of classical Rossby adjustment theory for an axisymmetric configuration corresponding to the laboratory experiments (figure 1). We use here an asymptotic expansion of the two-layer model, to extend the reduced gravity model studied by Flierl (1979) and Killworth (1992) in which the motion in the lower layer was neglected. We assume here that:

(i) Viscosity and dissipative effects are negligible;

(ii) Each layer follows the rotating shallow-water equation under the reduced-gravity approximation;

(iii) The system reaches a final steady state.

One of the main concerns about using the shallow-water model is its simplification of the vertical flow structure, especially during the initial stages of adjustment (see figure 3, for instance) and in the frontal region where the upper layer thickness vanishes to zero. The discrepancy or the agreement of this simple model with the experiments will be analysed in §6.

In order to obtain a dimensionless set of equations, we use h_0 as a vertical scale and R_d as a horizontal scale. Besides, for the upper (deep lower) layer we use $2\Omega_0 R_d (\delta 2\Omega_0 R_d)$ as a velocity scale and $\rho_0 g^* h_0 (\delta \rho_0 g^* h_0)$ as a pressure scale.

If we look for an axisymmetric steady state, which is the solution of the shallow-water equations, we necessarily obtain a radially symmetric motion in cyclo-geostrophic balance in both layers (index 1 for the upper and 2 for the lower)

$$\frac{v_1^2}{r} + v_1 = \partial_r \pi_1, \tag{4.1}$$

$$\delta \frac{v_2^2}{r} + v_2 = \partial_r \pi_2, \tag{4.2}$$

and the pressure continuity at the interface gives

$$\pi_1 - \delta \pi_2 = h, \tag{4.3}$$

where h is the dimensionless thickness of the upper layer. Then, the Lagrangian conservation of potential vorticity (PV) implies a constant value of PV for all fluid parcel within the upper lens:

$$q_1(r \leqslant r_f) = 1 = \frac{1 + \partial_r v_1 + v_1/r}{h}, \tag{4.4}$$

where r_f is the final radius of the density lens. While, in the lower layer, there are two regions of constant PV

$$q_2(r \leqslant r_2) = \frac{\delta}{1 - \delta} = \delta \frac{1 + \delta(\partial_r v_2 + v_2/r)}{1 - \delta h}, \tag{4.5}$$

$$q_2(r > r_2) = \delta = \delta \left(\frac{1 + \delta(\partial_r v_2 + v_2/r)}{1 - \delta h} \right), \tag{4.6}$$

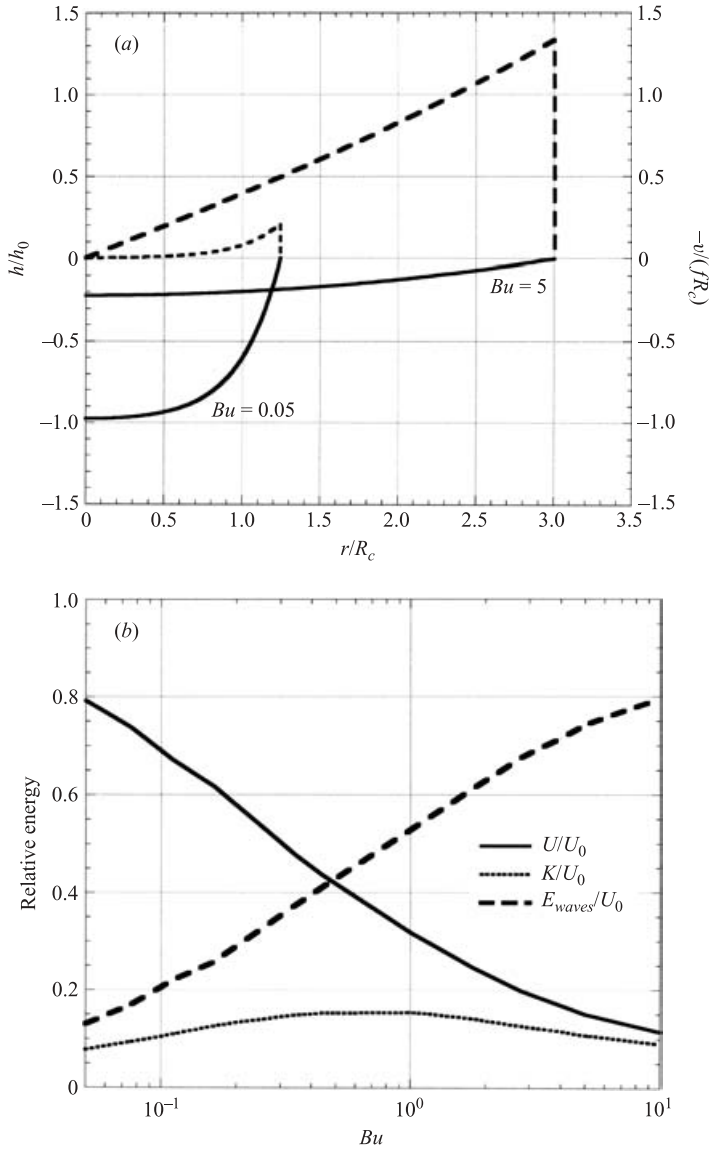where r_2 is the final radius of the PV jump.

FIGURE 3. Final steady state according to the standard adjustment model §4. (a) Two adjusted velocity (dashed line) and height (solid line) profiles resulting from the same initial density anomaly ($h = h_0, r = R_c$) are plotted for two different deformation radii $Bu = 0.05$ and $Bu = 5$. (b) Relative potential U/U_0, kinetic K/U_0 and wave energy E_{wave}/U_0 of the final adjusted state as a function of the Burgers number.

At the first order of expansion, for small $\delta \ll 1$ the upper layer does not feel the lower layer and according to (4.1), (4.3) and (4.5) we obtain an equation on v_1 independent of v_2

$$\frac{1}{r}\partial_r(r\partial_r(rv_1)) - \frac{v_1}{r^2} - \left(v_1 + \frac{v_1^2}{r}\right) = 0, \tag{4.7}$$

with the boundary conditions

$$v_1(r=0)=0, \tag{4.8}$$

$$h(r=r_f)=0 \Rightarrow \left(\partial_r v_1 + \frac{v_1}{r} + 1\right)(r=r_f)=0. \tag{4.9}$$

For a given radius r_f, we can solve (4.7), (4.8) and (4.9) numerically with standard shooting methods. Then, the angular momentum conservation or mass conservation both give the same implicit relation between r_f and the initial radius of the cylinder r_c:

$$r_c^2 = r_f^2 + 2r_f v_1(r_f). \tag{4.10}$$

For small δ, the lower layer is controlled by the upper-layer dynamic. The radial displacement of fluid (order δ) can be neglected and therefore according to (4.5) and (4.6) we obtain

$$\partial_r v_2 + v_2/r = 1 - h > 0 \quad (r \leqslant r_c), \tag{4.11}$$

with

$$v_2(r=0)=0, \tag{4.12}$$

and

$$\partial_r v_2 + v_2/r = -h < 0 \quad (r > r_c), \tag{4.13}$$

with

$$v_2(r \geqslant r_f)=0. \tag{4.14}$$

Hence, the velocities v_1, v_2 and the height $h(r)$ profiles of the adjusted density lens are fixed by a single parameter $r_c = R_c/R_d = Bu^{-1/2}$, provided that $\delta \ll 1$. Examples of velocities and height profiles are given in figure 3(*a*) for the same initial state and two different deformation radii corresponding to $Bu = 0.05$ and $Bu = 5$. For small Burgers number we expect an axisymmetric jet (or large-scale ring) whereas for large Burgers number an eddy (close to solid rotation) is expected.

Once we obtain v_1, v_2 and h, the relative potential and kinetic energy of the steady adjusted state can be calculated using

$$\frac{U}{U_0} = 2Bu \int_0^{r_f} h^2 r \, dr, \tag{4.15}$$

$$\frac{K}{U_0} = 2Bu \left[\int_0^{r_f} v_1^2 h r \, dr + \delta \int_0^{r_2} v_2^2 (1 - \delta h) r \, dr \right], \tag{4.16}$$

where $U_0 = \pi \rho_0 g^* h_o^2 R_c^2$ is the initial energy of the system. A simple energy budget, calculated at the first order in δ,

$$\frac{U_0 - E}{U_0} = 2Bu \left[\int_0^{r_c} r \, dr - \int_0^{r_f} (h^2 + h v_1^2) r \, dr \right] = -2Bu \int_0^{r_f} h v_1 r^2 \, dr > 0, \tag{4.17}$$

shows that there is an energy deficit between the available potential energy U_0 and the final energy $E = U + K$ of the adjusted lens. Hence, the steady solution given by (4.4), (4.5) and (4.6) cannot be an exact solution of the problem and time-dependent motion must be examined. In standard adjustment theory, fast components of motion, especially inertia-gravity waves, are expected to contain the missing part of the energy (Gill 1982). The repartition between potential U/U_0, kinetic K/U_0 and wave energy E_{wave}/U_0 is plotted in figure 3(*b*). For small Burgers number, there is a weak
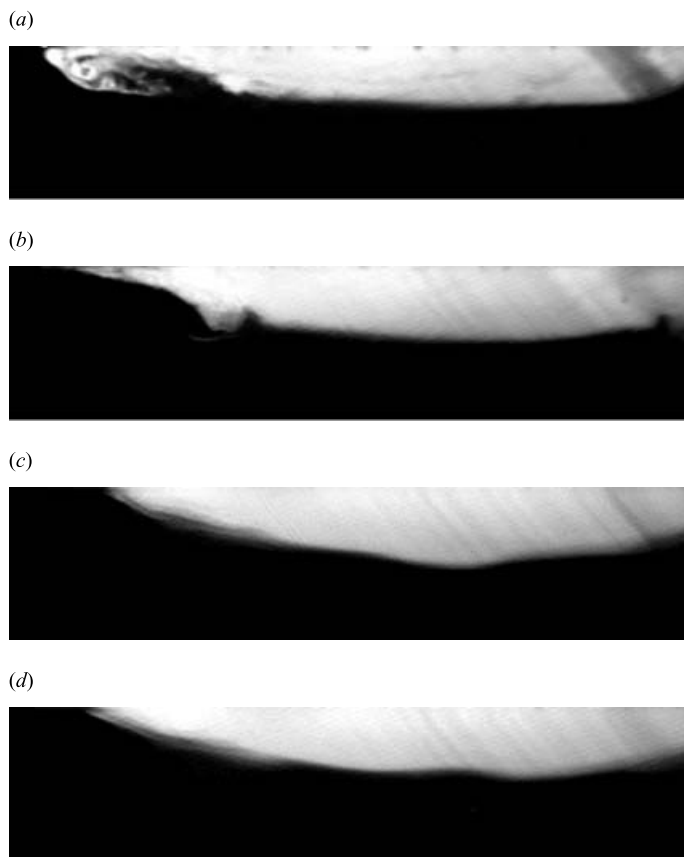
(*a*)

(*b*)

(*c*)

(*d*)

FIGURE 4. Dynamical evolution of the density anomaly (vertical cross-section) corresponding to $h_0 = 2.5$ cm, $R_c = 5.25$ cm, $H = 30$ cm, $\Omega_0 = 0.96$ rad s^{-1} and $\Delta\rho/\rho = 0.016$. The dark rays on the right-hand side of the image are experimental shadows produced by the upper fixations of the cylinder. (*a*) $t = 0.5T_f$, (*b*) $0.8T_f$, (*c*) $3T_f$, (*d*) $3.4T_f$.

energy transfer from the initial potential energy to the wave energy, while for large Burgers number, the initial energy is almost totally transferred to the wave energy.

5. Stages of geostrophic adjustment

Three stages were observed during the adjustment process. Just after the rapid withdrawal of the transparent cylinder, the fresh water spreads radially in a similar way to the gravity current (figure 4*a*). During this initial stage, the flow is fully three-dimensional and the effects of rotation are expected to be weak. After approximately half the inertial period $T_f = \pi/\Omega_0$, the radial extension of the density front is stopped. Similar results were found by Ungarish & Huppert (1998) and Hallworth, Huppert & Ungarish (2001) for rotating axisymmetric bottom gravity currents and Bouruet-Aubertot & Echevin (2002). By means of numerical and laboratory investigations, they found that the maximum radius of the front is first attained at $t \sim 0.5$–$0.85T_f$. Once the maximum propagation is achieved, we observe in our experiment a strong reverse flow close to the front. This second stage corresponds to a radial contraction of the density anomaly. During this contraction, steep jumps in the interface (analogous in their shape to hydraulic jump or shock) may appear (figure 4*b*). Identical features

were also observed in the Navier–Stokes numerical simulations labelled VIR-1 in Hallworth *et al.* (2001). After about two inertial periods T_f, the density front reaches an equilibrium characterized by standing wave mode superimposed on a mean state (figure $3c, d$). The amplitude of these oscillating modes could be small or large depending on the initial state.

The characteristic time of the first two stages described above does not depend on the Burgers number Bu or the front steepness α. In all our experiments, the third stage, corresponding to a mean adjusted state coupled with standing oscillating modes, is rapidly reached after approximately one or two inertial periods of rotation. These results agree with Mahalov *et al.* (2000) who also found that the inertial period T_f is the characteristic time of the transition from a bottom density current to a geostrophic front.

In the present experiments, the interface between the two fluids intersects the free surface. Hence, unlike the standard Rossby adjustment problem (Gill 1982) inertia–gravity waves cannot propagate away from the region of the initial density anomaly. Therefore, the separation between the adjusted state and the wave motion is not direct. However, using a time averaging at one or two T_f, we can separate the slow dynamics of the mean profile and the fast dynamics of the oscillating modes.

6. Mean adjusted state

In this section, we analyse the slow dynamics of the density anomaly averaged over one inertial period $T_f = \pi/\Omega_0$. This temporal averaging filters out the fast dynamics on both the density interface and the azimuthal velocity. The mean state obtained after two inertial periods is then compared to the prediction of the standard adjustment model described in §4. According to this model the adjustment is controlled by a single parameter: the Burger numbers Bu. Hence, we perform several experiments varying only the Burgers number while the steepness parameter $\alpha = 0.7$–0.8 and the depth ration δ remain constant.

6.1. *Profile of the density interface*

The averaged profiles of the density interface are displayed in figure 5 for different values of the Burgers number $Bu = 0.048$, 0.4 and 1. We plot the mean interface at two different times: at $t \sim 2T_f$ just after the withdrawal of the cylinder and five to ten inertial periods later. We observe that the mean density profile remains approximately constant during this period. Hence, even if a perfect steady state cannot be obtained for long times (10–$100T_f$) owing to the Ekman decay, the horizontal viscous dissipation or the baroclinic instability, the mean profile of the mass anomaly reaches a quasi-equilibrium state from approximately $2T_f$ to $10T_f$. The averaged density profile measured at this stage is in correct agreement with the adjusted state calculated in §4.

However, to quantify more precisely the accuracy of the adjustment model for various values of the Burgers number, we use two dimensionless lengths that characterize the shape of the mean adjusted profile. The first one is the ratio h/h_0 in the centre of the lens, where h is the mean thickness of the adjusted profile at $r = 0$ and h_0 the initial thickness of the density anomaly. The second one is the relative front displacement d/Rd, where $d = R_f - R_c$ is the difference between the radius of the adjusted lens R_f and R_c the initial radius of the density anomaly. According to figure 6, the thickness of the adjusted lens is predicted well by the standard adjustment
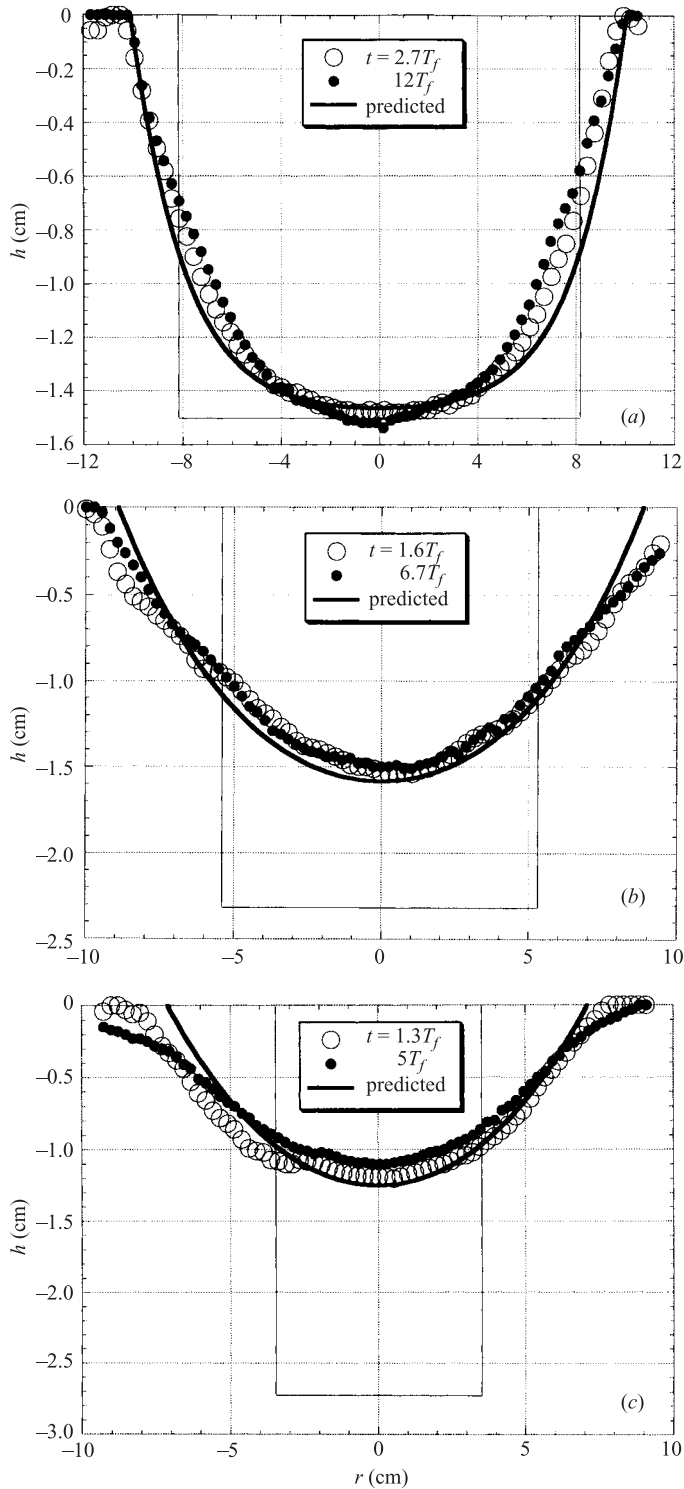
FIGURE 5. Mean profile of the density interface averaged over one inertial period for (*a*) $Bu =$ 0.048, (*b*) 0.4 and (*c*) 1. The initial state confined within the cylinder is plotted with a thin solid line while the cyclo-geostrophic adjusted state predicted by the standard scenario of adjustment is plotted with a thick solid line.
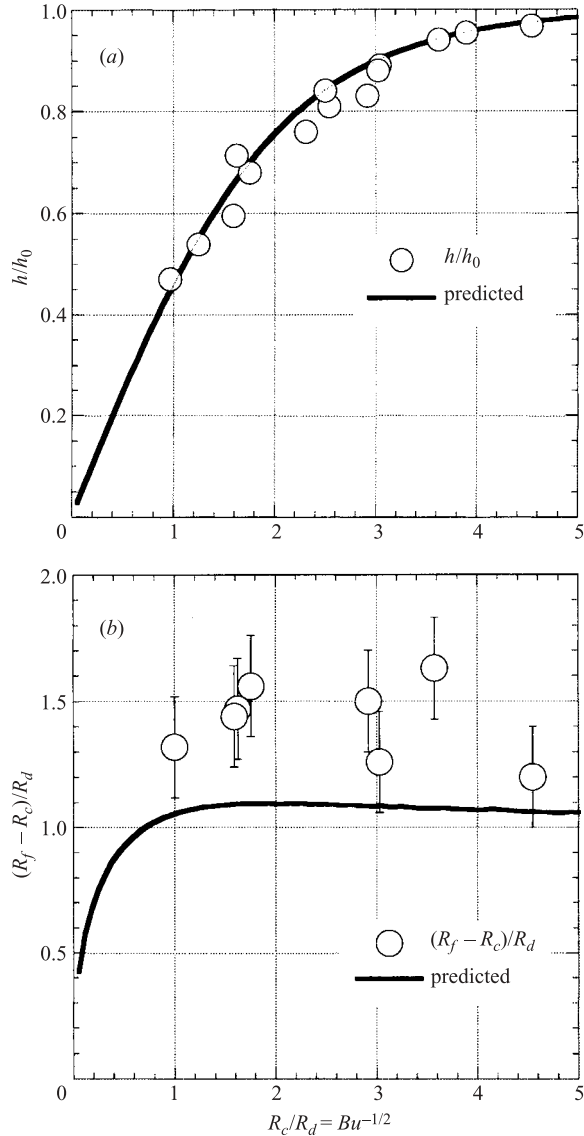
FIGURE 6. (*a*) Relative lens thickness h/h_0 at $r = 0$ and (*b*) relative front propagation $(R_f - R_c)/R_d$ compared with the standard adjustment model (thick solid line) at various Burgers numbers, $h_0(R_c)$ is the initial thickness (radius) of the density anomaly.

(figure 6*a*) while the radial extension of the front is underestimated by the inviscid model (figure 6*b*).

6.2. *Azimuthal velocity*

Typical particle trajectories averaged over one inertial period, at $t = 2T_f$ after the withdrawal of the cylinder, are displayed in figure 7(*a*). The mean motion is axisymmetric and the angular momentum conservation implies an anticyclonic velocity profile in the upper lens (figure 7*b*). Besides, we detected a cyclonic motion in the deep lower layer which was one order of magnitude smaller than the motion in the upper lens. We check here that we could reasonably neglect the lower-layer
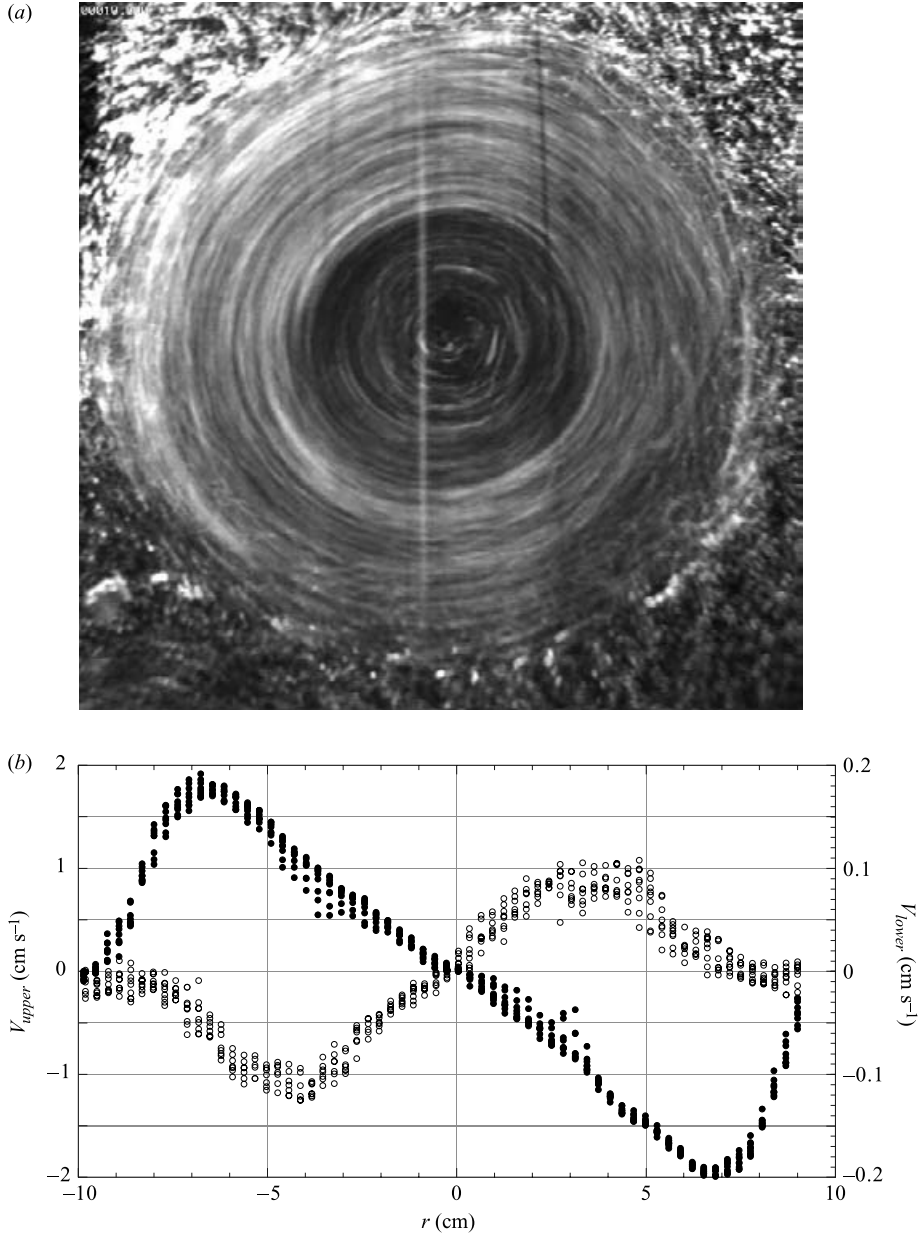
(a)

(b)

FIGURE 7. (a) Particle trajectories averaged over 1 s for $Bu = 0.4$, $\delta = 0.08$ and $\alpha = 0.69$ showing a strong axisymmetric motion within the density patch, with almost no velocity outside. (b) The orthoradial velocities are obtained from CIV processing in the upper lens and the deep lower layer. ●, upper layer; ○, lower-layer.

velocities during the stages of adjustment. This approximation is made in the reduced gravity model used for the cyclo-geostrophic adjustment formulated in §4.

The averaged velocity profiles in the lens are displayed in figure 8 for various Burgers numbers $Bu = 0.11, 0.4$ and 1. According to the inviscid adjustment model the velocity reaches its maximum and is discontinuous at the edge of the front, this is obviously unrealistic in a physical system where dissipative processes occur.
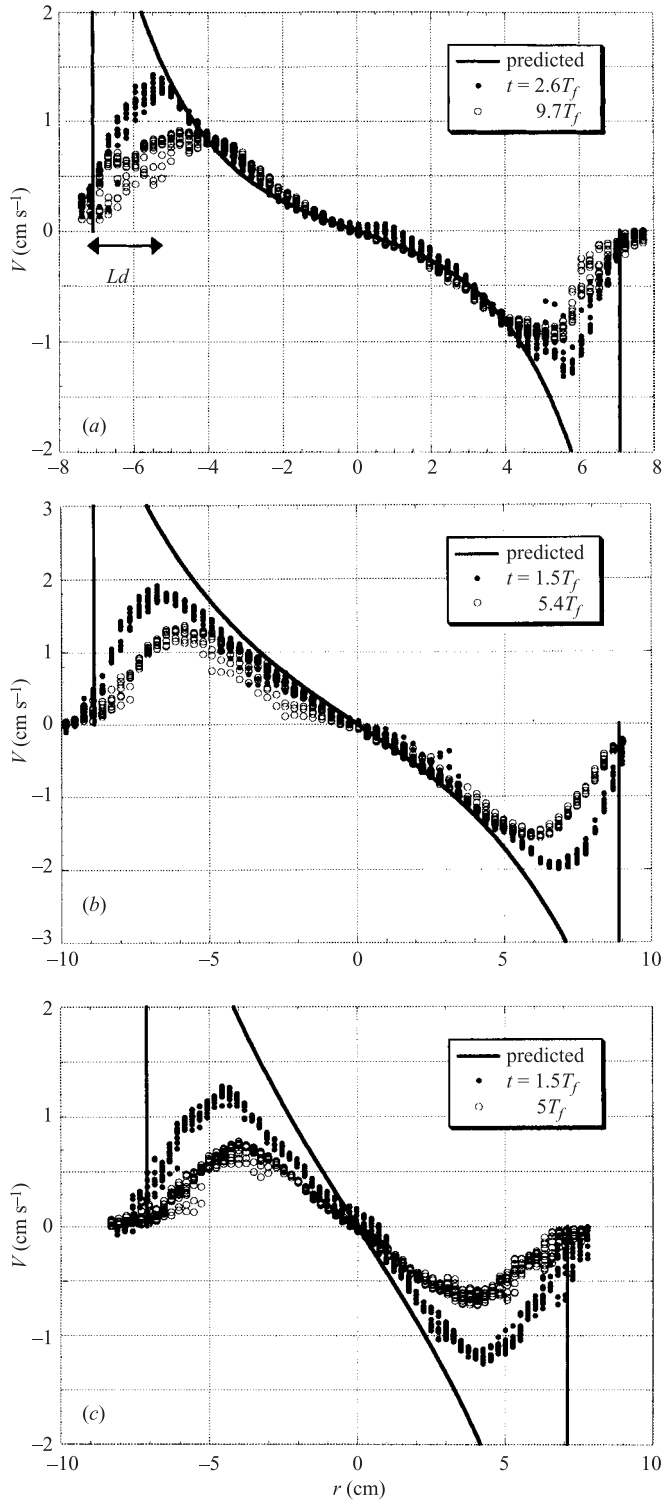
FIGURE 8. Mean velocity profiles within the density anomaly (5 mm below the free surface) averaged over one inertial period for (*a*) $Bu = 0.11$, (*b*) 0.4 and (*c*) 1. The cyclo-geostrophic adjusted state predicted by the standard scenario of adjustment is plotted with a thick solid line.

The maximum velocity observed in the laboratory experiment was not located at the edge of the density front and its amplitude was smaller than the predicted one (only 30%–40% according to our measurements). To understand what could be the main dissipative mechanism involved here, we look at the characteristic length of the decreasing velocity region L_d. According to the figure 8, this latter scales with the deformation radius $R_d = \sqrt{g^* h_0}/2\Omega_0$ which is much larger (1.7–3.5 cm in the present experiment) than the horizontal viscous diffusion length $L_v = \sqrt{\nu T_f}$ (2–4 mm). Hence, the velocity profile is not smoothed by a standard horizontal dissipation, a Laplacian operator for instance. Besides, L_d remains almost constant for a few inertial periods and does not follow a diffusive law such as $L_d^2 \propto t$. Therefore, it seems that the main dissipation occurs during the first stage of adjustment. Indeed, L_d scales with R_d, which is the characteristic scale of the front propagation.

In order to estimate the vorticity within the lens, we fit the velocity profile with an order-nine polynomial. Then, we derive the fitting polynomial to obtain the cylindrical vorticity

$$\omega(r) = \partial_r v + \frac{v}{r}. \tag{6.1}$$

We display, in figure 9(*a*), the profile of the local Rossby number deduced from the polynomial fit,

$$R_0 = \frac{v(r)}{2\Omega_0 r} \tag{6.2}$$

and, in figure 9(*b*) the profile of the dynamical Rossby number constructed with the vorticity:

$$\epsilon = \frac{\omega(r)}{2\Omega_0}. \tag{6.3}$$

The local Rossby number R_0 estimates the amplitude of the centrifugal force with respect to the Coriolis force in the cyclo-geostrophic balance (4.1). As expected for small Burgers numbers, curvature effects tend to be small and we can neglect the centrifugal term. In other words, the mean steady state is expected to become close to a geostrophic balance when R_c is large in comparison with R_d. Note that R_0 is small (below 0.1) for the case $Bu = 0.11$, while it reaches a moderate value (0.15–0.2) for $Bu = 1$ (figure 8*a*).

The dynamical Rossby number ε estimates the amplitude of the relative vorticity $\omega(r)$ with respect to $f_0 = 2\Omega_0$. According to figure 9(*b*), this latter term is of finite value and the central part of the lens is surrounded with a ring of cyclonic vorticity (i.e. a shielded vortex). The isolated nature of the lens, no circulation outside the density anomaly, implies this cyclonic vorticity ring. Nevertheless, the finite value of the dynamical Rossby number could strongly affect the frequency range and the structure of inertia–gravity waves present within the density anomaly (see Part 2, Stegner *et al.* 2004). Besides, it was shown (Stegner & Dritschel 2000) that ε is a key parameter which controls the ageostrophic effects in the one-and-a-half rotating shallow-water model. When the dynamical Rossby number is of order 1 a cyclone–anticyclone asymmetry affects the growth rate of unstable modes. The departure from geostrophy, in this reduced gravity model, tends to make anticyclonic structures less unstable than cyclonic ones.

6.3. *Cyclo-geostrophic balance and non-hydrostatic effects*

An important issue of this study was to characterize, for the mean adjusted state, the balance between the velocity and the density fields observed in the laboratory
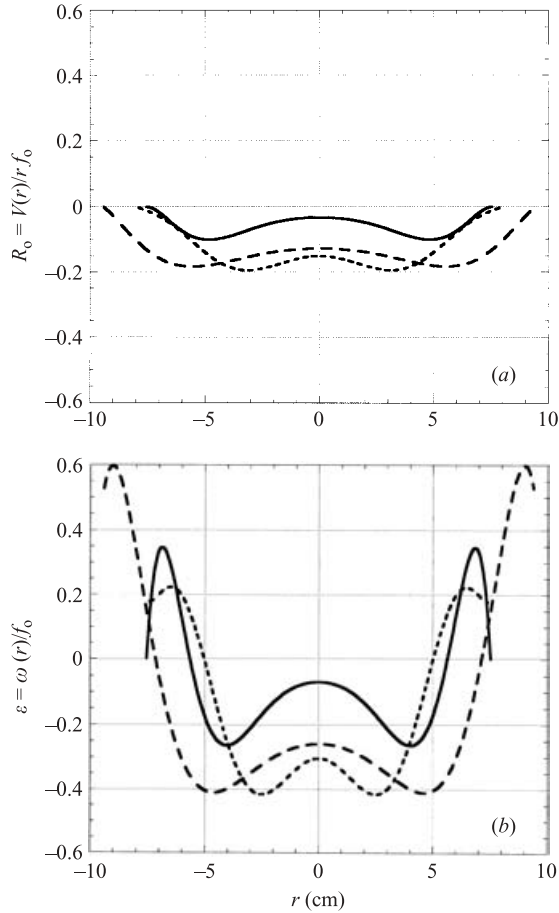
FIGURE 9. (*a*) Local Rossby number and (*b*) dynamical Rossby number obtained from a nine-order polynomial fit of the velocities profiles plotted in figure 7. ——, $Bu = 0.11$; - - -, 0.4; -·-, 1.

experiments. The double laser sheet set-up described in §2 was necessary to obtain quantitative and simultaneous measurements of the horizontal velocity and the density lens profile. According to figures 5 and 8 the mean adjusted state is not in perfect agreement, especially the velocity field, with the steady state predicted by the classical Rossby adjustment theory (§4). Nevertheless, this mean adjusted state could follow a perfect geostrophic or cyclogeostrophic balance defined by (4.2).

We could ask about the error made when one of the two fields (height or velocity) is inferred from the second one according to a prescribed balance relation. On one hand, we compared, in figure 10(*b*), the measured velocity profile with the geostrophic and the cyclogeostrophic velocities derived from the best polynomial fit of the density lens profile, figure 10(*a*). Such types of reconstruction are often used in oceanic data analysis where direct velocity measurement obtained from buoy trajectories or local current-meter are sparse. Therefore, the velocity field is generally reconstructed according to geostrophic or quasi-geostrophic balance from salinity and temperature fields measured at a higher resolution. In our laboratory experiments, according to figure 10(*b*), such reconstructed velocities overestimated the real velocity in the frontal
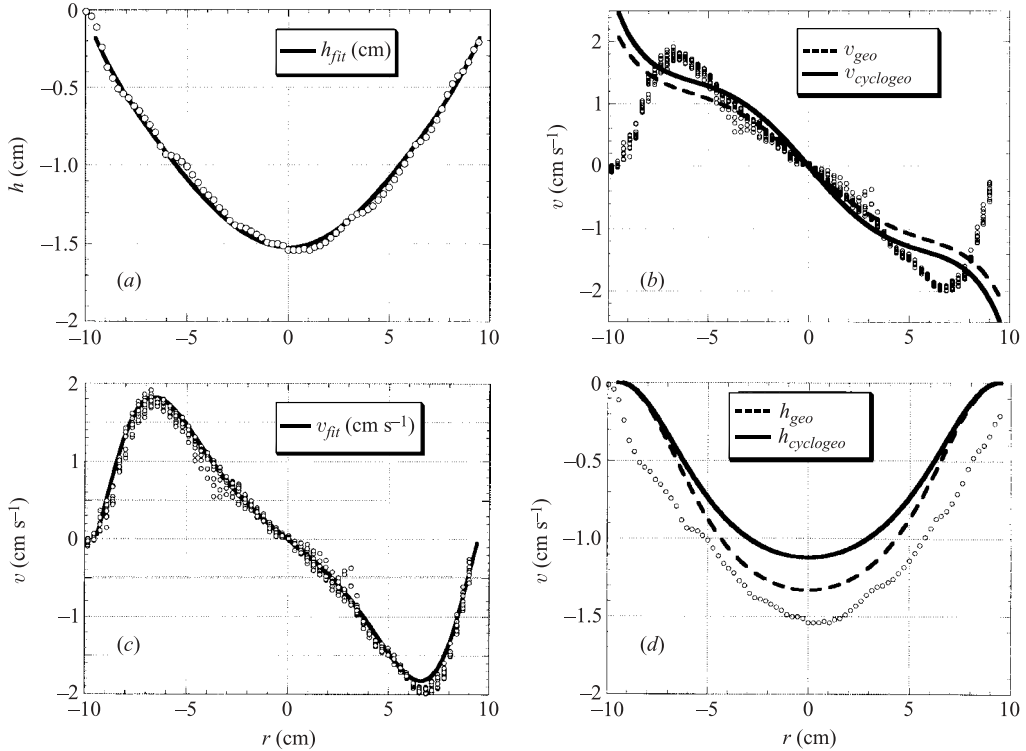
FIGURE 10. (*b*) Measured velocity in comparison with the cyclo-geostrophic or geostrophic velocity profile deduced from (*a*) the observed height profile. (*d*) Measured density profile in comparison with the cyclogeostrophic or geostrophic height profile deduced from (*c*) the observed velocity profile. 0, $t = 1.5 T_f$.

region and the extension of the cyclonic vorticity region is poorly reproduced. On the other hand, if we reconstruct the lens profile (figure 10*d*) from the polynomial fit of the velocity profile (figure 10*c*) we underestimate the thickness of the density anomaly. Hence, the mean adjusted state does not follow an exact geostrophic or cyclogeostrophic balance.

In order to quantify the deviation from the cyclogeostrophic balance we calculate the following error function:

$$e(r) = \frac{g^*}{f_0} \partial_r h - v - \frac{v^2}{r f_o}. \tag{6.4}$$

We compared the amplitude of the error function with the horizontal velocity. According to figure 11, the deviation from the cyclogeostrophic balance becomes significant close to the frontal region where the density interface intersects the free surface. These strong values of the error function indicate that the horizontal pressure gradient does not follow the hydrostatic equation (4.3) in the frontal region. This discrepancy could result either from non-hydrostatic motions or from the limit of validity of the shallow-water layer formulation. On one hand, we do not observe steady non-hydrostatic motion leading to significant vertical and radial flows. Hence, the only non-hydrostatic motions are related to (unsteady) internal wave activity, which could lead to irreversible breaking events in the frontal region. Such mechanisms transfer
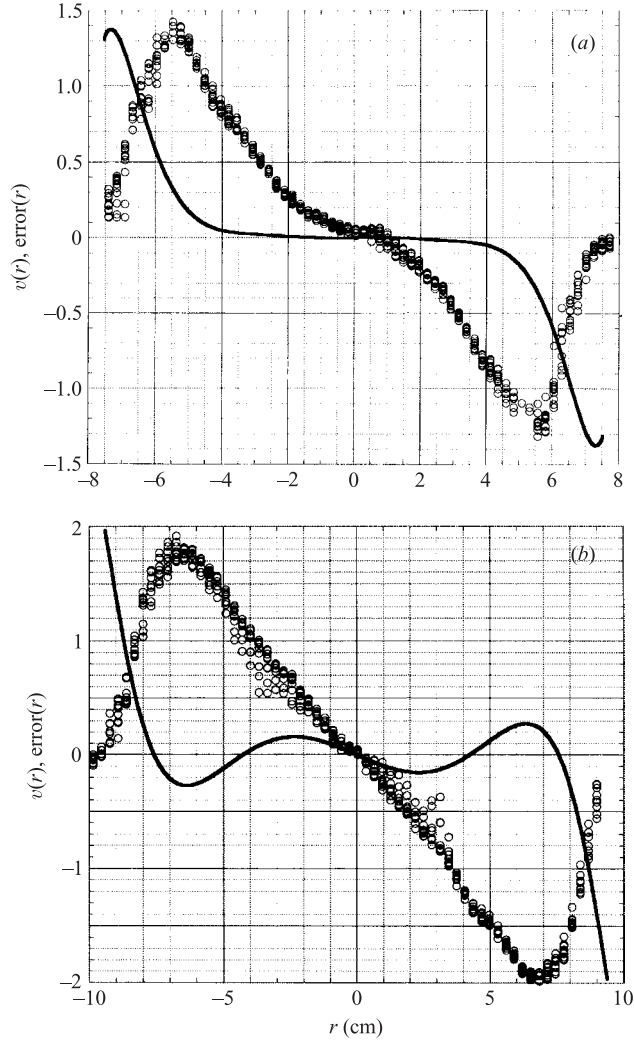
FIGURE 11. Deviation from cyclogeostrophic balance for (a) $Bu = 0.11$ and (b) 0.4. —, error function on velocity (equation (6.4)), ○, measured velocity.

horizontal momentum to the mean flow and therefore could induce a forcing term in the balanced momentum equation (4.1). On the other hand, at the edge of the density anomaly the upper-layer thickness vanishes and therefore we cannot neglect the thickness of the interface $d\rho$ in comparison with h_0. For instance, if we consider the case $Bu = 0.4$ (figures 5b and 8b), in the frontal region when the velocity reaches its maximum value ($r \sim 7$ cm) $d\rho \sim 3$ mm while $h \sim 7$ mm. Hence, the continuous density stratification should be taken into account which implies significant deviation from the pressure balance (4.3) and the two-layer shallow-water formulation. However, according to the spatial and temporal resolution of experimental measurements, we can hardly quantify the vertical variations of the density and velocity fields in the frontal region. Thus, we could hardly distinguish between these two possible explanations.
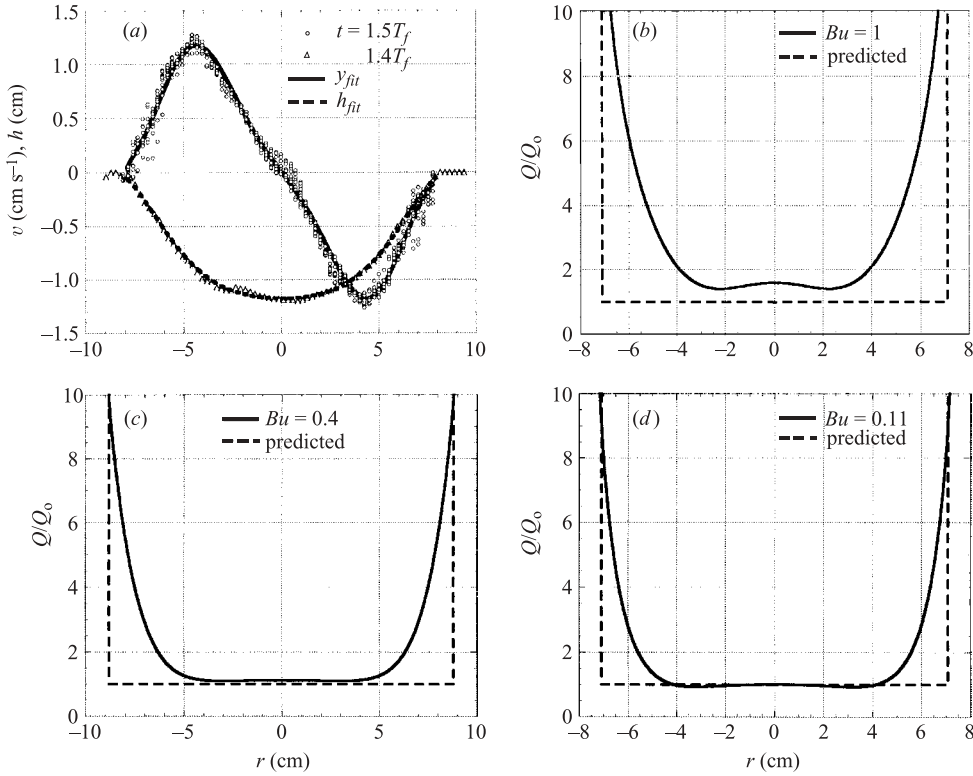
FIGURE 12. Potential vorticity profiles for (*b*) $Bu = 1$, (*c*) 0.4 and (*d*) 0.11, deduced from independent measurements of velocity and height fields. These two profiles are fitted with high-order polynomials (*a*). - - -, PV profiles predicted by standard adjustment (§4); —, profiles measured in the experiment.

6.4. *PV conservation*

The conservation of potential vorticity is the keystone of geostrophic adjustment theory (Rossby 1938; Obukhov 1949; Blumen 1972) which provides a means for the determination of an adjusted state from a given initial state (see §4). As far as we know, this conservation principle was never checked in laboratory experiments. Hence, we focus our efforts to obtain the PV profile after adjustment using independent measurements of both the horizontal velocity field and the vertical density field. First, we fit these two axisymmetric fields with a high-order polynomial (figure 12*a*). Then, we calculate, according to the fitting polynomial, the vorticity and the PV profile for various Burgers number (figure 12). In the low Burgers limit, when the front displacement remains small in comparison with the initial size, the PV is conserved in the centre of the density anomaly (figure 12*c*, *d*). However, for all cases, dissipation occurs in the frontal region. Note that a deficit of anticyclonic vorticity leads to an increasing PV. Hence, even if the PV has higher values (solid line) than the PV predicted by the inviscid adjustment model (dashed lines), it is the result of a dissipative process. In fact, the PV gradients are smoother than the predicted ones.

We can also note that all the PV profiles in figure 12 are very close to monotonic. Nevertheless, for large Burger number (figure 12*b*) there is an inflection point in the PV. This is due to the cyclonic vorticity ring, observed in the experiments (figure 11), which induces at least one inflection point in the vorticity profile close to the centre.

Bu	$\dfrac{U}{U_0}$ (measured)	$\dfrac{U}{U_0}$ (predicted)	$\dfrac{K}{U_0}$ (measured)	$\dfrac{K}{U_0}$ (predicted)
0.11	0.715	0.66	0.045	0.107
0.4	0.497	0.46	0.076	0.151
1	0.37	0.32	0.03	0.148

TABLE 1. Energy budget of the mean adjusted flow.

For small Burgers numbers, the PV is dominated by the density profile $h(r)$, while for large Burgers number the PV is mainly controlled by the vorticity $\omega(r)$. Hence, we expect an inflection point in the PV profile for finite Bu. Therefore, according to the generalization of the Rayleigh instability criterion for the quasi-geostrophic model, such a density anomaly having a non-monotonic PV profile could be unstable to barotropic disturbances. Of course, for intermediate shallow-water $\alpha = 0.4 - 1.2$ and a finite value of the dynamical Rossby number $\varepsilon = 0.2 - 0.4$ the quasi-geostrophic model is not strictly valid. However, it gives a first-order approximation of the slow dynamics. This could explain why Griffiths & Linden (1981) never found a stable density anomaly in their experiments even for large Burgers number where large-scale baroclinic disturbances are (in principle) not unstable. In this case, the inflection point in the PV profile could be the source of a mixed barotropic–baroclinic instability. Besides, we can also note that the dynamical Rossby number reaches a finite value ($\varepsilon \sim 0.4$) for large Bu ($Bu = 1$). Hence, short-scale ageostrophic gravity-Rossby instabilities (Hayashi & Young 1987; Sakai 1988; Paldor & Ghil 1991; Boss *et al.* 1996) could be dominant when the large-scale baroclinic instability cannot occur.

7. Energy budget and transient dissipative mechanisms

The quantitative energy budget and the estimate of the fraction of the initial energy which is transferred to the wave motion is the strong result of the standard Rossby adjustment theory (§ 4). In laboratory experiments, as in oceanic or atmospheric flows, dissipation and three-dimensional motions could change this energy budget significantly. In order to quantify the energy dissipation that occurs during the adjustment, we need to measure precisely the potential, the kinetic and the wave energy.

The potential and kinetic energy of the mean adjusted state were calculated from the measured density and velocity profiles (figures 5 and 8) according to equations (4.15) and (4.16). On one hand, the potential energy of the mean adjusted flow was very close to or slightly higher than the value predicted by the inviscid adjustment theory (see the data of table 1, corresponding to the three cases $Bu = 1$, 0.4 and 0.11). This is a direct consequence of the results presented in figure 5 where the experimental profiles of the density interface were in good agreement with the predicted ones. Besides, the mixing induced by the early stages of adjustment, see figure 4 for instance, tends to increase the potential energy of the system and could therefore explain the slight deviation of the potential energy measured in the experiments. On the other hand, the mean adjusted state exhibited a strong deficit of kinetic energy in comparison with the predicted one. This deficit increases with the Burgers number (from 50% to 70%) and is directly related to the smoothed velocity profile plotted figure 8. Indeed, in the experiments, unlike the Rossby adjustment prediction (§ 4), the maximum velocity

Bu	$\dfrac{\Delta U}{U_0}$ (measured)	$\dfrac{E_{waves}}{U_0}$ (predicted)	$\dfrac{E_{dissipated}}{U_0}$ (estimated)
0.11	0.117	0.233	0.123
0.4	0.175	0.3890	0.252
1	0.09	0.532	0.51

TABLE 2. Estimate of the wave energy and dissipation.

was not located at the edge of the density front and its amplitude was significantly reduced. An estimation of the energy accumulated in the oscillatory wave motion is required to conclude whether the missing kinetic energy was dissipated or transferred to the wave motion.

Assuming that the wave energy, released during the adjustment, corresponds mainly to rapid quasi-inertial oscillations of the density interface we compute the maximum fluctuation of the potential energy according to (4.15). The oscillations of the density profile are of finite amplitude and in phase opposition with the oscillations of the velocity profile (see Part 2 for more details). The energy is then periodically transferred from potential to kinetic energy. Hence, if we just measure the potential energy fluctuation, we expect to quantify the whole wave energy. The latter and the wave energy predicted from the standard Rossby adjustment are compared in table 2. Here again, we measured a strong deficit in energy (50% to 80%) which increased with the Burgers number. Hence, a significant fraction of the initial energy is both missing in the wave energy and the mean kinetic energy of the adjusted state. A simple budget of the potential, the kinetic and the wave energy measured in the experiment gives an estimate of the dissipation in the early stage of adjustment. As was discussed in §6.2, the molecular viscosity cannot explain the rapid dissipation (less than $2\,Tf$) of such large fractions (12%–50%) of the initial energy.

A rapid barotropic instability, previously shown by Holford (1994), occurs at the edge of the density front and exhibits small-scale three-dimensional structures. This initial shear instability of the horizontal velocity at the edge of the density patch is probably the dominant mechanism which extracts kinetic energy of the flow. In order to visualize the rapid growth of small-scale asymmetric perturbations we performed a few experiments where a high concentration of blue organic dye (methylene blue) was introduced in to the upper fresh water. During the initial release of the cylinder, the density gradient was almost vertical and, when the density front just started to propagate radially, a strong horizontal velocity shear appeared. During this stage ($t = 0.1$–$0.2T_f$), a first unstable perturbation having a short wavelength grows very quickly (figure 13a). This wavelength is of the same order of magnitude as the viscous diffusion length $L_v = \sqrt{\nu T_f}$ (2–4 mm) which is expected to give the initial size of the velocity gradient. Then, as far as the density front propagates, the shear region increased. Hence, the velocity gradient and the interface slope are reduced. The wavelength of the azimuthal perturbation increased and spiralling rolls became visible (figure 13c). At this stage ($t \sim 0.5$–$0.7T_f$), when the density anomaly reached its maximum extension and started to reverse, we probably observed a combination of shear layer and Kelvin–Helmholtz instabilities. We can roughly estimate a Richardson number for the initial phase of adjustment

$$Ri = -\frac{g\partial_z\rho}{\rho(\partial_z V)^2} \approx \frac{g^* d}{V^2} \approx \frac{g^* h_0}{V^2}\frac{d}{h_0} \approx \frac{d}{h_0} \tag{7.1}$$
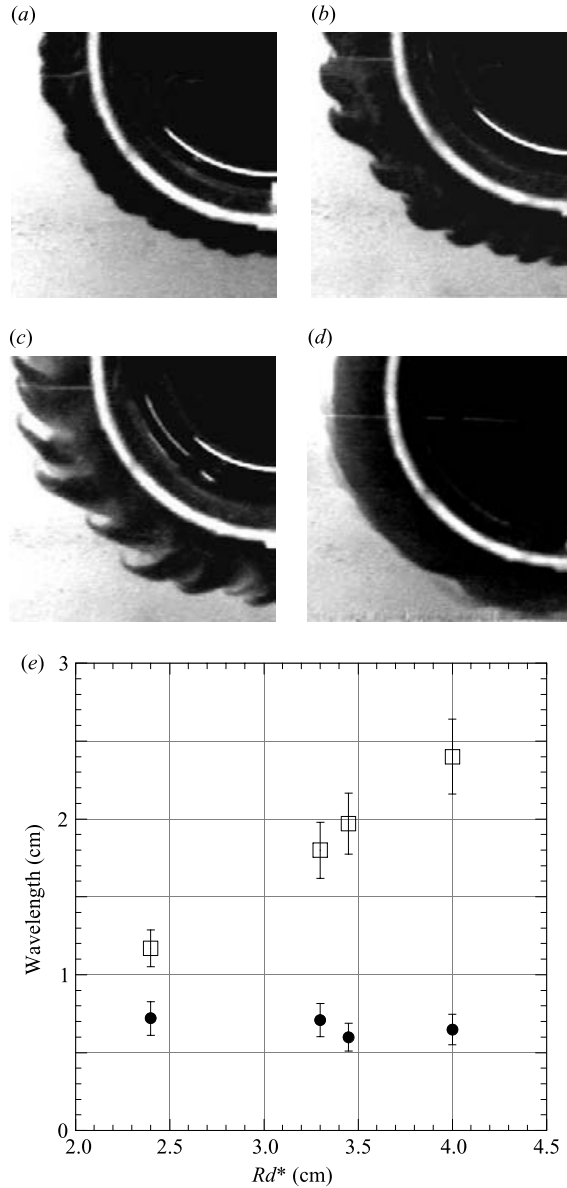
(*a*)   (*b*)

(*c*)   (*d*)

(*e*)

FIGURE 13. Dye visualization of azimuthal and three-dimensional perturbations at the initial stage of adjustment (*a*) $t = 0.3T_f$, (*b*) $0.5T_f$, (*c*) $0.7T_f$, to (*d*) $1.7T_f$. The parameters for this experiment were close to those of figure 4: $Bu = 0.4$, $\delta = 0.08$ and $\alpha = 0.7$. (*e*) The wavelength of the first perturbation ●, λ_{init} and the □, spiralling arms λ_{arms} are plotted versus the deformation radius.

assuming that the density front speed V satisfies a Froude number close to unity, which is generally the case for non-rotating density current. In this case, Ri is directly proportional to the ratio of the density gradient thickness d with the mean lens thickness h_0. Since d is smaller than h_0 (figure 2) this Richardson number could have, during the initial phase of adjustment, a small value below the threshold of Kelvin–Helmoltz instability. Unlike the initial perturbation, the wavelength of the
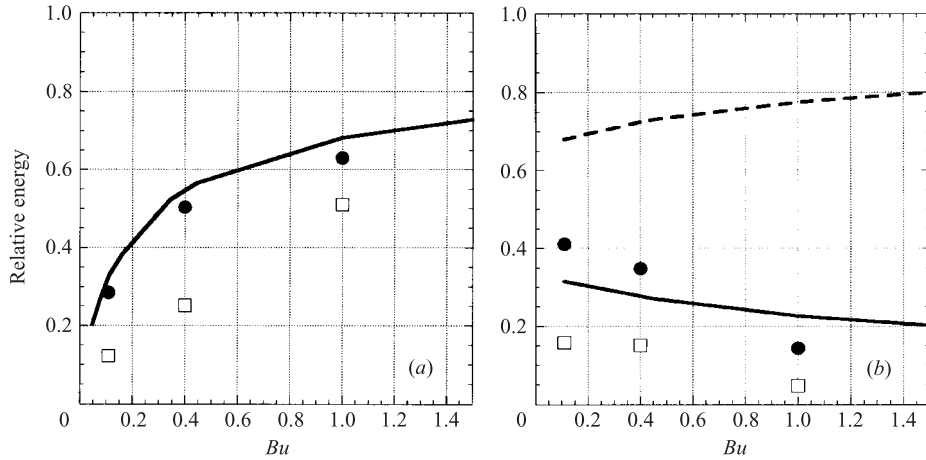
FIGURE 14. Repartition of $U_0 - U$ the potential energy released during the adjustment process. (*a*) Fraction of the initial energy transferred: ——, theoretical prediction; ●, experimental results; □, estimate of dissipation. (*b*) Repartition of the transferred energy to kinetic energy $K/(U_0 - U)$ (——, theory; □, experiment) and wave energy $E_{wave}/(U_0 - U)$) (- - -, theory; ●, experiment).

spiralling arms depends on the deformation radius (figure 13*e*). This latter is also the characteristic distance of the density front propagation. After the first oscillation of the mass anomaly (i.e. after one inertial period T_f) the three-dimensional perturbations disappeared and the flow was almost axisymmetric (figure 13*d*).

A high fraction of the initial potential energy released during the adjustment process is dissipated by these transient three-dimensional instabilities. Both the amount of energy transferred $1 - U/U_0$ and the energy dissipated E_{dissip}/U_0 increase with the Burgers number (figure 14*a*). The dissipation could affect up to 80% of the released energy. Hence, it strongly changes the energy budget predicted by the non-dissipative adjustment model based on Lagrangian conservation of PV. The influence of the Burgers number on the dissipation is emphasized when we look at the repartition of the mean flow kinetic energy and the wave energy (figure 14*b*). These two terms are well below the predicted values. We may note that the density front propagation $d = R_f - R_c$ (see figure 6) scales with the Rossby radius. Hence, the area where the three-dimensional perturbations grow, described in figure 13, increases with the deformation radius and the energy dissipation is then also expected to increase with the Burgers number.

According to the above analysis, the main dissipative mechanism that occurs during the adjustment process depends on the relative scale of the mass anomaly, the Burgers number. We may ask what other parameter could control the fraction of energy dissipated? On one hand, the molecular viscosity could play only a stabilizing role on the shear layer or the Kelvin–Helmholtz instabilities. Therefore, even if a weak effect of the Reynolds number Re could be found, we do not expect a significant reduction of dissipative processes for higher Re that are reached in larger-scale experiment or in the atmosphere and the oceans. On the other hand, the front steepness α was of finite value and kept constant in the experiments. This parameter is expected to control the amplitude of non-hydrostatic and three-dimensional motions. Therefore, it could affect the fraction of energy dissipated during the transient instabilities.

8. Conclusion

We investigated the nonlinear cyclo-geostrophic adjustment of a circular density front in a two-layer fluid. This configuration corresponds to a rapid input of potential energy in a geostrophic fluid layer. We focused our efforts on the visualization techniques in order to have simultaneous and independent measurements of both the horizontal velocity field and the vertical density field. We thus obtained, for the first time, quantitative measurements on the potential vorticity, the flow balance and gave an estimate of the energy budget after a geostrophic adjustment process.

Surprisingly, even if during the early stage of adjustment, strong three-dimensional motions (plume structures, shocks and rapid transient instabilities) occur, the density profile and the potential energy of the mean adjusted state observed in the experiments are in good agreement with the prediction of the standard non-dissipative adjustment theory. This results from the fact that dissipative effects are significant in the frontal region only. Therefore, the potential vorticity conservation is verified except in this region.

Nevertheless, the transient and three-dimensional instabilities that occur during the very first stage of adjustment are an efficient mechanism of turbulent dissipation which rapidly cascades energy toward small scales in the frontal region. This mechanism strongly changes the velocity and the energy budget predicted by the standard Rossby adjustment theory. These three-dimensional motions localized in time (less than one inertial period) and space (edge of density front) could dissipate up to 50% of the initial energy of the system. Both the kinetic energy of the mean adjusted state and the energy transferred to inertia–gravity waves modes are significantly reduced by these dissipative processes. Hence, we have shown here that, for a rapid input of energy, the adjustment process cannot be separated from the development of small-scale barotropic instabilities. In such cases, the energy transferred to the non-geostrophic wave motion will be generally overestimated by the standard adjustment principle or by general circulation models where subgrid dissipation is difficult to parameterize. Therefore, it would be interesting to investigate further the rapid barotropic instability observed during the initial stage of the adjustment as well as the effect of wave breaking in the frontal region in order to provide an accurate parameterization of these processes. Our results indicate that the energy dissipated varies like the Burgers number. We are at present investigating further the energy budget using direct numerical simulations.

This experimental study provides some insights on rapid adjustment processes that occur in the ocean for instance in upwelling fronts, meso-scale eddies like warm core rings (e.g. Csanady 1979; Flierl 1979) and possibly during the spreading phase of dense water observed during convective events. In particular, Flierl (1979) used a frontal eddy model assuming a PV patch and cyclo-geostrophic equilibrium for warm core eddies. Such a dynamical structure, which exhibits a strong velocity shear at the edge of the density anomaly, will necessarily experience three-dimensional instabilities in the frontal region as in our experiments. Flierl (1979) has shown that while theoretical predictions are in good agreement with the interface profile of the observed warm core eddies, they overestimate the observed velocities. This discrepancy is similar to our results, even if the warm core eddy of the Gulf Stream experiences probably a weaker dissipation than the one generated by the dam-break adjustment. Hence, an eddy model assuming both a discontinuity in the velocity and the potential vorticity is not realistic for oceanic vortices. In such a case, the classical scenario of geostrophic adjustment is strongly modified and the mean adjusted state cannot satisfy the PV conservation in the frontal region. Nevertheless, we could ask if a

standard frontal model assuming just a PV discontinuity, with a continuous velocity profile (Gill 1982; McWilliams 1988; Boss & Thompson 1995; Kuo & Polvani, 2000) could reach an adjusted state without experiencing three-dimensional dissipation. Laboratory investigations on the adjustment of these smoother density fronts are under progress.

REFERENCES

BLUMEN, W. 1972 Geostrophic adjustment. *Rev. Geophys. Space Phys.* **10**, 485.

BOURUET-AUBERTOT, P. & ECHEVIN, V. 2002 The influence of the coast on the dynamics of upwelling fronts. Part II: Numerical simulations. *Dyn. Atmos. Oceans* **36**, 175–200.

BOURUET-AUBERTOT, P. & LINDEN, P. F. 2002 The influence of the coast on the dynamics of upwelling fronts Part I: Laboratory experiments. *Dyn. Atmos. Oceans* **36**, 153–173.

BOSS, E., PALDOR, N. & THOMPSON, L. 1996 Stability of a potential vorticity front: from quasi-geostrophy to shallow-water. *J. Fluid Mech.* **315**, 65–84.

BOSS, E. & THOMPSON, L. 1995 Energetics of nonlinear geostrophic adjustment. *J. Phys. Oceanogr.* **25**, 1521–1529.

CSANADY, G. T. 1979 The birth and death of a warm core ring. *J. Geophys. Res.* **82**, 777–780.

DEWAR, W. K. & KILLWORTH, P. D. 1990 On the cylinder collapse problem, mixing and the merger of isolated eddies. *J. Phys. Oceanogr.* **20**, 1563–1575.

FLIERL, G. R. 1979 A simple model for the structure of warm cold core rings. *J. Geophys. Res.* **82**, 781–785.

FORD, R., NORTON, W. A. & McINTYRE, M. E. 2000 Balance and the slow quasimanifold: some explicit results. *J. Atmos. Sci.* **57**, 1236–1254.

GILL, E. 1982 *Atmosphere–Ocean Dynamics.* Academic. pp 662.

GRIFFITHS, R. W. & LINDEN, P. F. 1981 The stability of vortices in a rotating, stratified fluid. *J. Fluid Mech.* **105**, 283–316.

HALLWORTH, M. A., HUPPERT, H. E. & UNGARISH, M. 2001 Axisymmetric gravity currents in a rotating system: experimental and numerical investigations. *J. Fluid Mech.* **447**, 1–29.

HAYASHI, Y. Y. & YOUNG, W. R. 1987 Stable and unstable shear modes of rotating parallel flows in shallow water. *J. Fluid Mech.* **184**, 477–504.

HOLFORD, J. M. 1994 The evolution of a front. PhD thesis, University of Cambridge.

KILLWORTH, P. D. 1992 The time-dependent collapse of a rotating fluid cylinder. *J. Phys. Oceanogr.* **22**, 390–397.

KUO, A. C. & POLVANI, L. M. 1997 Time-dependent fully nonlinear geostrophic adjustment. *J. Phys. Oceanogr.* **27**, 1614.

KUO, A. C. & POLVANI, L. M. 1999 Wave–vortex interaction in rotating shallow-water. Part 1. One space dimension. *J. Fluid Mech.* **394**, 1–27.

KUO, A. C. & POLVANI, L. M. 2000 Nonlinear geostrophic adjustment, cyclone/anticyclone asymmetry, and potential vorticity rearrangement. *Phys. Fluids* **12**, 1087–1100.

McWILLIAMS, J. C. 1988 Vortex generation through balanced adjustment. *J. Phys. Oceanogr.* **18**, 1178–1192.

MAHALOV, A., PACHECO, J. R., VOROPAYEV, S. I. *et al.* 2000 Effects of rotation on fronts of density currents. *Phys. Lett.* A **270**, 149–156.

OBUKHOV, A. M. 1949 On the question of the geostrophic wind. *Izv. Akad. Nauk SSSR, Geogr. Geofiz.* **13**, 281.

PALDOR, N. & GHIL, M. 1991 Shortwave instabilities of coastal currents. *Geophys. Astrophys. Fluid Dyn.* **58**, 225–241.

REZNIK, G. M., ZEITLIN, V. & BENJELLOUL, M. 2001 Nonlinear theory of geostrophic adjustment. Part 1. Rotating shallow-water model. *J. Fluid Mech.* **445**, 93–120.

ROSSBY, C. G. 1938 On the mutual adjustment of pressure and velocity distribution in certain simple current systems II. *J. Mar. Res.* **1**, 239–263.

SAKAI, S. 1998 Rossby–Kelvin instability: a new type of ageostrophic instability caused by a resonance between Rossby waves and gravity waves. *J. Fluid Mech.* **202**, 149–176.

STEGNER, A., BOURUET-AUBERTOT, P. & PICHON, T. 2004 Nonlinear adjustment of density fronts. Part 2. In preparation.

STEGNER, A. & DRITSCHEL, D. G. 2000 A numerical investigation of the stability of isolated shallow-water vortices. *J. Phys. Oceanogr.* **30**, 2562–2573.

UNGARISH, M. & HUPPERT, H. E. 1998 The effect of rotation on axisymmetric gravity currents. *J. Fluid Mech.* **362**, 17–51.

VERZICCO, R., LALLI, F. & CAMPANA, E. 1997 Dynamics of baroclinic vortices in a rotating, stratified fluid: a numerical study. *Phys. Fluids* **9**, 419–432.

ZEITLIN, V., MEDVEDEV, S. & PLOUGONWEN, R. 2003 Frontal geostrophic adjustment, slow manifold and nonlinear wave phenomena in one-dimensional rotating shallow water. Part 1. Theory. **481**, 269–290.